

Article

Monometallic and Bimetallic Catalysts Supported on Praseodymium-Doped Ceria for the Water–Gas Shift Reaction

Weerayut Srichaisiriwech and Pannipa Tepamatr *

Department of Chemistry, Faculty of Science and Technology, Thammasat University, Pathumthani 12120, Thailand; weerayut@tu.ac.th

* Correspondence: pannipa@tu.ac.th

Abstract: The water–gas shift (WGS) performance was investigated over 5%Ni/CeO₂, 5%Ni/Ce_{0.95}Pr_{0.05}O_{1.975}, and 1%Re4%Ni/Ce_{0.95}Pr_{0.05}O_{1.975} catalysts to decrease the CO amount and generate extra H₂. CeO₂ and Pr-doped CeO₂ mixed oxides were synthesized using a combustion method. After that, Ni and Re were loaded onto the ceria support via an impregnation method. The structural and redox characteristics of monometallic Ni and bimetallic NiRe materials, which affect their water–gas shift performance, were investigated. The results show that the Pr addition into Ni/ceria increases the specific surface area, decreases the ceria crystallite size, and improves the dispersion of Ni on the CeO₂ surface. Furthermore, Re addition results in the enhancement of the WGS performance of the Ni/Ce_{0.95}Pr_{0.05}O_{1.975} catalyst. Among the studied catalysts, the ReNi/Ce_{0.95}Pr_{0.05}O_{1.975} catalyst showed the highest catalytic activity, reaching 96% of CO conversion at 330°. It was established that the occurrence of more oxygen vacancies accelerates the redox process at the ceria surface. In addition, an increase in the Ni dispersion, Ni surface area, and surface acidity has a positive effect on hydrogen generation during the water–gas shift reaction due to favored CO adsorption.

Keywords: Re; hydrogen production; water–gas shift; bimetallic catalyst



Citation: Srichaisiriwech, W.; Tepamatr, P. Monometallic and Bimetallic Catalysts Supported on Praseodymium-Doped Ceria for the Water–Gas Shift Reaction. *Molecules* **2023**, *28*, 8146. <https://doi.org/10.3390/molecules28248146>

Academic Editors: Jorge Sambeth, Miguel Andrés Peluso and Jorge Colman Lerner

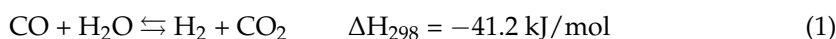
Received: 13 October 2023
Revised: 8 December 2023
Accepted: 14 December 2023
Published: 18 December 2023



Copyright: © 2023 by the authors. Licensee MDPI, Basel, Switzerland. This article is an open access article distributed under the terms and conditions of the Creative Commons Attribution (CC BY) license (<https://creativecommons.org/licenses/by/4.0/>).

1. Introduction

Water–gas shift (WGS) reaction is an industrial technology that involves the reaction of water vapor and carbon monoxide to generate H₂ and CO₂. The water–gas shift reaction takes place according to the following equation:



The development of H₂ and fuel cell technologies provides numerous advantages such as high-efficiency power, environmentally friendliness, and sustainability. WGS reactions have received widespread attention to increase the H₂ concentration in the syngas. Hydrocarbon reforming can produce syngas that consists of CO, H₂, H₂O, and CO₂. However, a trace concentration of CO poisons the catalysts utilized in fuel cells [1]. Precious metal-based proton exchange membrane fuel cell anodes require a carbon monoxide amount in the inlet gas below 10–20 ppm; otherwise, the anode is poisoned [2]. A purification process is required to decrease the CO concentration lower than the cell tolerance level after hydrogen is produced via the reforming process of carbon-containing molecules (such as hydrocarbons or alcohols). The advantage of using the WGS reaction is to reduce CO content while generating more hydrogen as fuel for the H₂ fuel cell. The appearance of a suitable catalyst in the WGS reaction can reduce the CO content to 10 ppm.

The support plays a critical role in oxidation reactions such as water–gas shift reactions or CO oxidation. The utilization of redox-active oxides such as CeO₂ as a support material leads to superior catalytic efficiency compared to the use of other oxide support such as alumina or silica [3–6]. Due to its redox characteristics, CeO₂ can promote vacancy generation and water dissociation, which plays an important role in the catalytic performance of

water–gas shift reactions. However, pure CeO₂ has some disadvantages, like deactivation of the Ce⁴⁺/Ce³⁺ redox couple and thermal sintering, resulting in a reduction in its oxygen storage capacity (OSC) and catalytic performance [7]. Thus, many efforts have been dedicated to improving the reducibility and catalytic performance of CeO₂ by doping it with other cations to generate more oxygen vacancies and develop its resistance to thermal sintering [8,9]. In this part, doping CeO₂ with aliovalent (such as Eu³⁺, La³⁺, Gd³⁺, and Sm³⁺) cations [10–12] or isovalent (such as Zr⁴⁺, Hf⁴⁺, and Ti⁴⁺) cations [13,14] has been well described in the literature. The incorporation of an aliovalent cation into the CeO₂ lattice produces oxygen vacancies by charge compensation on the final oxide materials [15]. Conversely, the CeO₂ doping with isovalent cations also results in the enhancement of the redox properties of CeO₂. Therefore, the partial substitution of Ce⁴⁺ by Zr⁴⁺ causes a deformation in the CeO₂ lattice because of the lower ionic radius of isovalent cations such as Zr⁴⁺, deriving an enhancement in the OSC of CeO₂. Moreover, these two effects can also be combined in a single study when doping CeO₂ with variable oxidation states of lanthanide elements. In such cases, Tb [16] and Pr [17,18] are the most studied ones. The Pr addition into the CeO₂ lattice enhances both oxygen desorption and oxygen vacancy generation compared to pure CeO₂. This result is due to the lower binding energy of oxygen anions in Ce-Pr mixed oxides and the higher reduction potential of Pr⁴⁺/Pr³⁺ compared to Ce⁴⁺/Ce³⁺. Therefore, the Zr dopant induces a limited amount of oxygen vacancies into the CeO₂ lattice [19,20], whereas the Pr dopant leads to a greater concentration of oxygen vacancies [21]. These behaviors result in redox properties in the Ce-Pr mixed oxides being superior to those of other mixed oxides. In previous works, Ce-Pr-O mixed oxide supports were studied for WGS reaction. It was found that the optimum promoting effect of Pr appears at a low loading of 5 %wt. [22,23]. In addition, the catalytic activity of such oxides can be obviously improved by adding a small amount of transition metals (cobalt, chromium, copper, and nickel) [24–26]. Nickel combined with CeO₂-based oxides are cost-effective alternatives to expensive noble metal catalysts and are often more reactive than noble metals [27]. However, CO and CO₂ methanation are very common side reactions for these catalysts [28,29]. This behavior is usually tempered by the incorporation of a second active metal like platinum [30,31]. Rhenium might be a good choice for replacing Pt catalyst because of its good electrochemical properties, its cheaper price compared to platinum, and its sustainable source. Re is widely used as a second metal to form bimetallic catalysts. In recent years, the use of bimetallic catalysts has attracted much attention due to their excellent efficiency and capability [32–34]. The effect of rhenium on the WGS performance of Pt/TiO₂ and Pt/ZrO₂ catalysts has been investigated, and the results exhibited that rhenium addition induces an increase in the WGS activity of Pt catalysts. Rhenium acts as an anchor for the platinum particles to enhance the Pt dispersion. In addition, the redox process between Re⁴⁺ and Re⁷⁺ over the WGS reaction would promote CO oxidation on the Pt catalyst [35,36]. Our initial studying found that rhenium also enhanced the WGS activity when it was doped on Ni/CeO₂-based oxides [11,37,38]. Apart from enhancing the performance of the WGS reaction, Pt-Re/carbon has also been reported to be active in several reactions, such as the reforming process [23] and glycerol to syngas conversion [39]. Furthermore, in studying the catalytic activity of ReCo/Al₂O₃ for the Fischer–Tropsch reaction found that Re addition increased the reaction rate of the Co catalyst. Re has been shown to be a good promoter by facilitating the reduction rate of cobalt species and producing more available active Co metal sites to participate in the reaction [40].

In this work, the performance of Ni/CeO₂ and Ni/Ce_{0.95}Pr_{0.05}O_{1.975} catalysts for the water–gas shift reaction was studied. Additionally, the role of rhenium addition on the water–gas shift performance of Ni/Ce_{0.95}Pr_{0.05}O_{1.975} catalyst was also observed. Therefore, the utilization of Pr as a dopant and Re as a metal additive in this work to maximize the WGS performance. The physicochemical properties of monometallic and bimetallic catalysts were examined to clarify the key factors in increasing the catalytic activity using the following techniques: X-ray diffraction, BET surface area, NH₃ temperature

programmed desorption, H₂ temperature programmed reduction, Raman spectroscopy, and chemisorption techniques.

2. Results and Discussion

2.1. Catalysts Characterization

X-ray diffraction patterns of CeO₂, 5%Ni/CeO₂, 5%Ni/Ce_{0.95}Pr_{0.05}O_{1.975}, and 1%Re4%Ni/Ce_{0.95}Pr_{0.05}O_{1.975} were illustrated in Figure 1. It suggests that the diffraction peaks of all catalysts correspond well to CeO₂ phases with a cubic structure (Joint Committee on Powder Diffraction File No. 43-1002). In addition, the weak peaks at 2θ about 37.1°, 43.2° and 63.2° attributed to the NiO phases of Ni-based catalysts, suggesting that there was a small proportion of nickel oxide. The CeO₂ crystallite size of supported Ni catalysts was determined using the Debye–Scherrer equation (Table 1). The calcination of Ni/CeO₂ catalyst at a high temperature (650 °C) after impregnation of Ni onto ceria support leads to the aggregation of ceria crystallites; thereby, the surface area decreases with a growth in CeO₂ crystallite size. However, Pr addition into 5%Ni/CeO₂ results in a decrease in the ceria crystallite size together with an increase in a specific surface area. The diffraction peaks of Ni/Ce_{0.95}Pr_{0.05}O_{1.975} and ReNi/Ce_{0.95}Pr_{0.05}O_{1.975} appeared at lower diffraction angles compared with the diffraction peaks of Ni/CeO₂, indicating that Pr incorporation in the CeO₂ lattice enlarged unit cell. The enhancement of the unit cell for Ni/Ce_{0.95}Pr_{0.05}O_{1.975} when compared with Ni/CeO₂ is due to Ce⁴⁺ ions (0.097 nm) being replaced by larger Pr³⁺ ions (0.112 nm). Therefore, an oxygen vacancy is expected to be formed because Pr³⁺ incorporation in the CeO₂ lattice produces unbalanced charges and strain. On the other hand, the diffraction peaks of Ni/CeO₂ appeared at higher diffraction angles compared with the diffraction peaks of pure CeO₂ because of the lattice contraction after calcination at high temperatures. Nickel could not be incorporated into CeO₂ lattice due to the nature of impregnation synthesis but the reduction in the cell dimension because of the decomposition of surface hydroxyls during calcination at 650 °C.

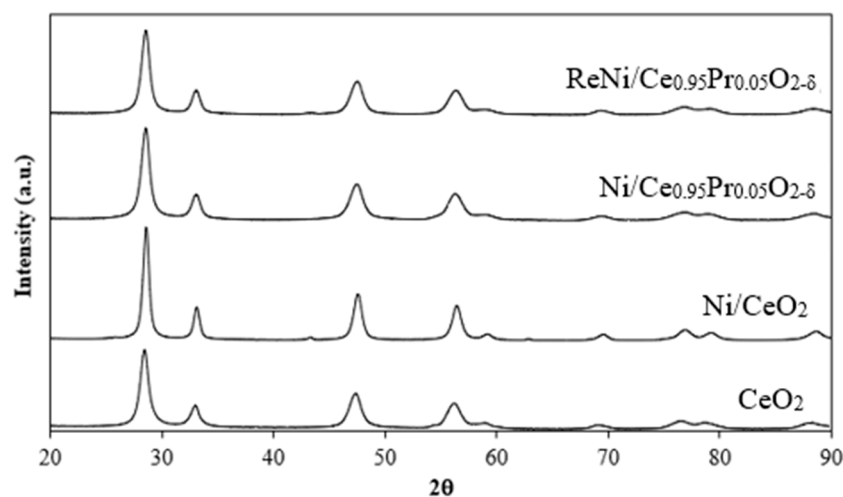


Figure 1. XRD patterns of Ni catalysts and CeO₂ support.

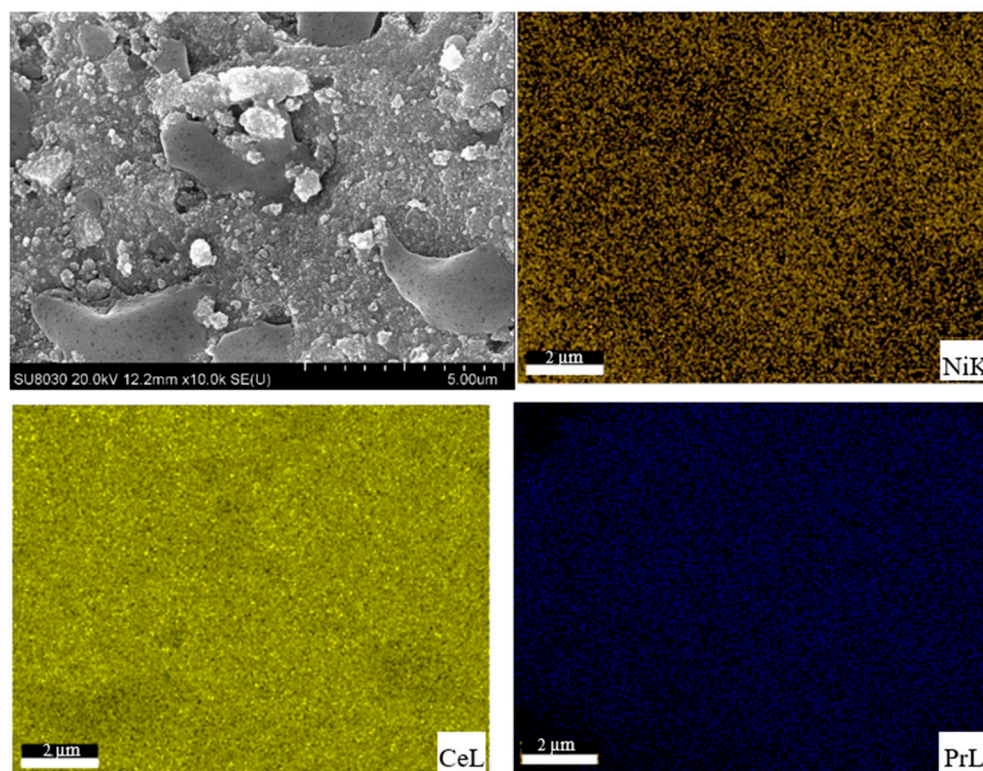
H₂ chemisorption analysis was used to determine the Ni dispersion of supported Ni catalysts. It was found that an addition of Pr to Ni/CeO₂ increases Ni dispersion on the catalyst surface. Moreover, rhenium impregnation onto Ni/Ce_{0.95}Pr_{0.05}O_{1.975} tremendously enhanced the dispersion and surface area of metallic nickel. This result may be due to the movement of electrons between Re, Ni, and CeO₂, which results in the formation of strong interaction between Ni metal and support; thereby, the metal dispersion and metal surface coverage enhances, whereas particle size reduces. 1%Re4%Ni/Ce_{0.95}Pr_{0.05}O_{1.975} exhibited the highest Ni surface area and dispersion among all the catalysts. Usually, a greater metal surface area provides more surface active sites exposed to reactants [36,37].

Table 1. BET surface area, crystallite size of CeO₂, Ni dispersion, and Ni surface area of Ni-based catalysts.

Catalysts	Crystallite Size ^a (nm)	BET Surface Area ^b (m ² /g)	Ni Dispersion ^c (%)	Ni Particle Size ^c (nm)	Ni Surface Area ^c (m ² /g)
CeO ₂	9.8	68	-	-	-
5%Ni/CeO ₂	13.35	45	0.17	35.1	0.95
5%Ni/CePrO	8.55	64	0.30	19.6	1.70
1%Re4%Ni/CePrO	8.01	60	1.15	5.50	6.08

^a Calculated from the 111 diffraction peak broadening. ^b Estimated from N₂ adsorption at −196 °C. ^c Estimated from H₂-chemisorption.

The chemical analysis by SEM micrographs with the corresponding elemental mapping was conducted to investigate the elemental distribution and the homogeneity of the supported Ni catalyst. As presented in Figure 2, Ce, Pr, and Ni elements were uniformly distributed on 5%Ni/Ce_{0.95}Pr_{0.05}O_{1.975} catalysts. The highly dispersed Ni suggests a strong metal–support interaction, and the enhancement in Ni dispersion would provide more active sites that are exposed to reactants, which is beneficial to the increase in WGS performance.

**Figure 2.** SEM image and elemental mapping of 5%Ni/Ce_{0.95}Pr_{0.05}O_{1.975}.

Raman spectroscopy was performed to quantify oxygen vacancies in the catalyst. CeO₂ catalyst initiates the water–gas shift process via a redox mechanism at high temperatures. CO adsorbs on the catalyst surface and subsequently oxidizes it with CeO₂ lattice oxygen to generate carbon dioxide and oxygen vacancy. H₂O oxidizes reduced CeO₂ again to produce H₂. A mechanism for increasing the catalytic performance of CeO₂ is the incorporation of dopant ions, with Pr³⁺ as a promising candidate dopant [41]. It is widely regarded that when doping CeO₂ with a trivalent cation, two Ce⁴⁺ ions in the CeO₂ lattice are substituted

by the dopants, and then an O ion is eliminated to conserve the charge [15]. Therefore, oxygen vacancy is directly related to catalytic activity in water–gas shift reaction.

As shown in Figure 3, a Raman peak near 460 cm^{-1} was attributed to a triple degeneracy active mode (F_{2g} peak), which represents the symmetrical stretching vibration generated by eight O atoms bound to one Ce atom. Secondary peaks at around 240 and 320 cm^{-1} characteristics of CeO_2 nanostructures are also found in $1\%\text{Re}4\%\text{Ni}/\text{Ce}_{0.95}\text{Pr}_{0.05}\text{O}_{1.975}$. In addition, another broad peak near 570 cm^{-1} (denoted by D peak) was associated with oxygen vacancies in CeO_2 [42,43]. The oxygen vacancies concentration can be represented by the ratio of $I_D/I_{F_{2g}}$ [44]. The intensity of the D peak in $1\%\text{Re}4\%\text{Ni}/\text{Ce}_{0.95}\text{Pr}_{0.05}\text{O}_{1.975}$ catalyst is stronger than that of other catalysts, indicating that higher oxygen vacancy concentration can be obtained by the addition of Re onto $\text{Ni}/\text{Ce}_{0.95}\text{Pr}_{0.05}\text{O}_{1.975}$ catalyst. Moreover, the presence of Ce^{3+} in the CeO_2 -based catalyst can be demonstrated by a red shift of the F_{2g} peak, which is due to the lattice expansion when Ce^{4+} ions (ionic radius 0.097 nm) are replaced by Ce^{3+} ions (ionic radius 0.114 nm) for oxygen vacancy formation [43,45]. The enhancement of oxygen vacancy concentration in the $1\%\text{Re}4\%\text{Ni}/\text{Ce}_{0.95}\text{Pr}_{0.05}\text{O}_{1.975}$ catalyst enables the interaction between rhenium, nickel, and CeO_2 to drive the metal dispersion and prevent the sintering of metal particles. This result indicates that the addition of Re to the $\text{Ni}/\text{Ce}_{0.95}\text{Pr}_{0.05}\text{O}_{1.975}$ catalyst improves the reducibility and stability.

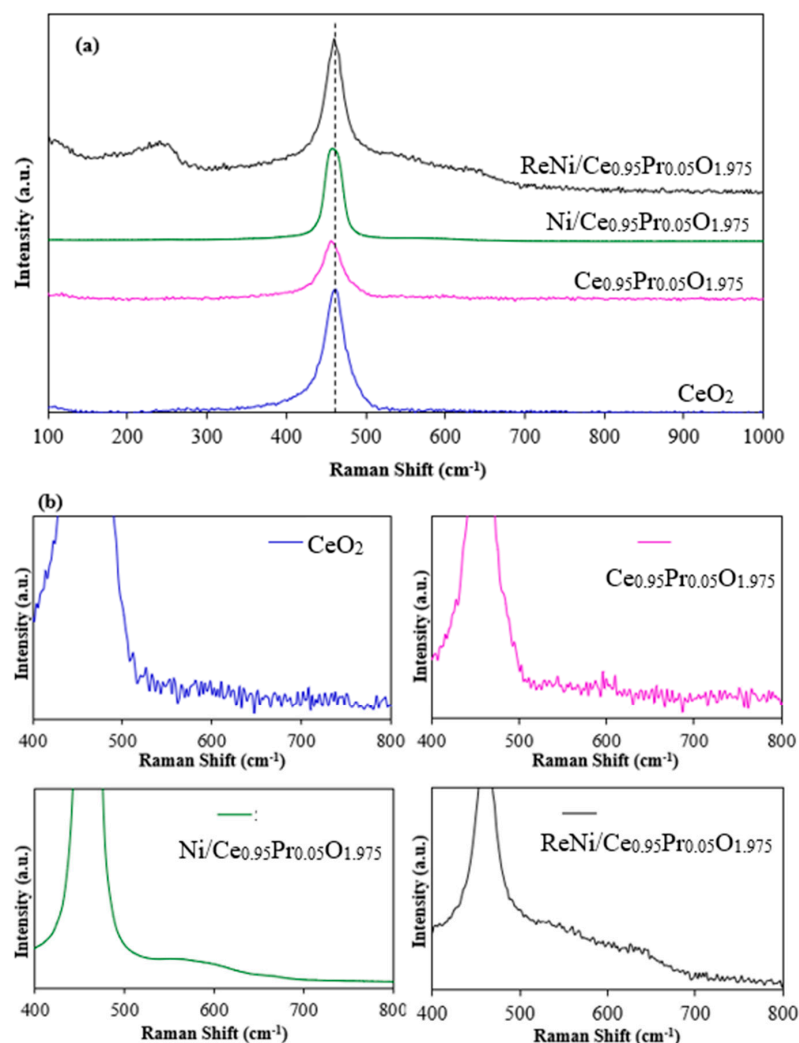


Figure 3. Raman spectra of CeO_2 support and Ni catalysts in the wide range of $100\text{--}1000\text{ cm}^{-1}$ (a) and the narrow range of $400\text{--}800\text{ cm}^{-1}$ (b).

The H₂-TPR profiles of CeO₂, 5%Ni/CeO₂, 5%Ni/Ce_{0.95}Pr_{0.05}O_{1.975}, and 1%Re4%Ni/Ce_{0.95}Pr_{0.05}O_{1.975} catalysts are shown in Figure 4. The H₂-TPR of CeO₂ exhibits two broad peaks at 500 °C and 750 °C. The peak at 500 °C is assigned to the reduction of surface-capping oxygen of CeO₂, and the peak at 750 °C is assigned to the bulk CeO₂ reduction. The TPR profile of the Ni/CeO₂ catalyst is characterized by a low-temperature peak at 272 °C, medium temperature at 345 °C, and bulk reduction at 830 °C. The reduction peak at 272 °C is assigned to the reduction of nickel oxide species. The consumption peak at 345 °C is assigned to the Ni-catalyzed reduction of the CeO₂ surface [46,47]. It is interesting to note that the incorporation of Ni to CeO₂ support significantly shifts the reduction peak of surface CeO₂ from 500 °C to 345 °C. The H₂-TPR of Ni/Ce_{0.95}Pr_{0.05}O_{2-δ} presented two nickel oxide reduction peaks at 220 °C and 278 °C, which was due to the different environments of Ni. The peak at 220 °C is probably due to the reduction of Ni in the vicinity of CeO₂, whereas the consumption peak at 278 °C is due to the presence of Pr. The reduction peak of surface and bulk species of Ni/Ce_{0.95}Pr_{0.05}O_{1.975} appeared at the same position as the reduction of Ni/CeO₂. This indicated that the addition of Pr to Ni/CeO₂ alters the NiO reduction behavior. The H₂-TPR profile of the bimetallic ReNi is different from those of monometallic Ni supported on Pr-doped CeO₂. In this case, electron density transfers between Re, Ni, Ce, and Pr may occur. As the result of electron density transfer, a concurrent reduction of metal oxide species was found, and reduction of metal oxide is easier. A stronger interaction between nickel and CeO₂ is expected to tune the nickel dispersion. The reduction peak appearing at a higher temperature normally means that it is more difficult to reduce with stronger metal–support interactions [48]. For the 1%Re4%Ni/Ce_{0.95}Pr_{0.05}O_{1.975} catalyst, stronger metal–support interactions are presented, which proved that the reduction of the surface shell of CeO₂ occurred at a higher temperature. The stronger interaction between metal and support is beneficial to maintain the metal dispersion and hinder its aggregation.

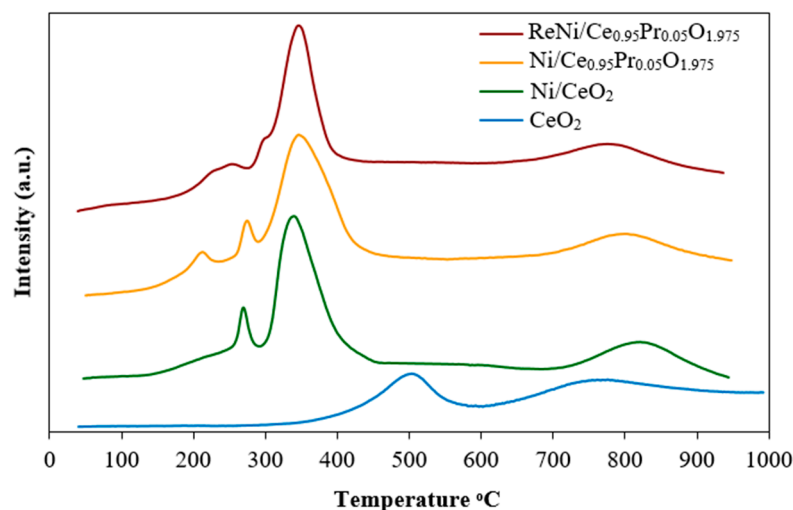


Figure 4. H₂-TPR profiles of monometallic Ni and bimetallic NiRe supported by pure CeO₂ and Pr-doped CeO₂.

The surface acidity of the prepared catalysts was studied using temperature-programmed desorption of ammonia (Figure 5), and the total acidity was estimated from the area under the NH₃ desorption peak. NH₃-TPD analysis was carried out in order to clarify the effect of the acidity of ReNi/Ce_{0.95}Pr_{0.05}O_{1.975} and Ni/Ce_{0.95}Pr_{0.05}O_{1.975} on the catalytic performance in the water–gas shift reaction. The peaks were assigned to weak, medium, or strong acid sites when falling in the 100–200 °C, 200–450 °C, or 450–700 °C temperature range, respectively. Increased surface acidity enabled a higher content of CO adsorption on the catalyst surface since a CO reactant in the WGS process is a weak base, explaining the observed increase in catalyst activity. Furthermore, the acidic character of the Ni catalyst

surface proved to be beneficial for CO₂ desorption, leaving behind free active sites for carbon monoxide and H₂O adsorption in subsequent reaction cycles [49]. The result from NH₃-TPD analysis indicates that the addition of Re onto Ni/Ce_{0.95}Pr_{0.05}O_{1.975} increases the concentration of weak-strength acid sites (peak area increases at <200 °C). In addition, the total concentration of surface acid sites can be estimated by integrating the NH₃-TPD curves, and it was found to be 41 and 28 mols/g for 1%Re4%Ni/Ce_{0.95}Pr_{0.05}O_{1.975} and 5%Ni/Ce_{0.95}Pr_{0.05}O_{1.975}, respectively. The obtained results could imply a higher tendency for carbon monoxide adsorption and subsequently easier CO₂ desorption on the bimetallic ReNi supported by Pr-doped CeO₂ surface, thereby the overall water–gas shift reaction rate over ReNi/Ce_{0.95}Pr_{0.05}O_{1.975} may be enhanced.

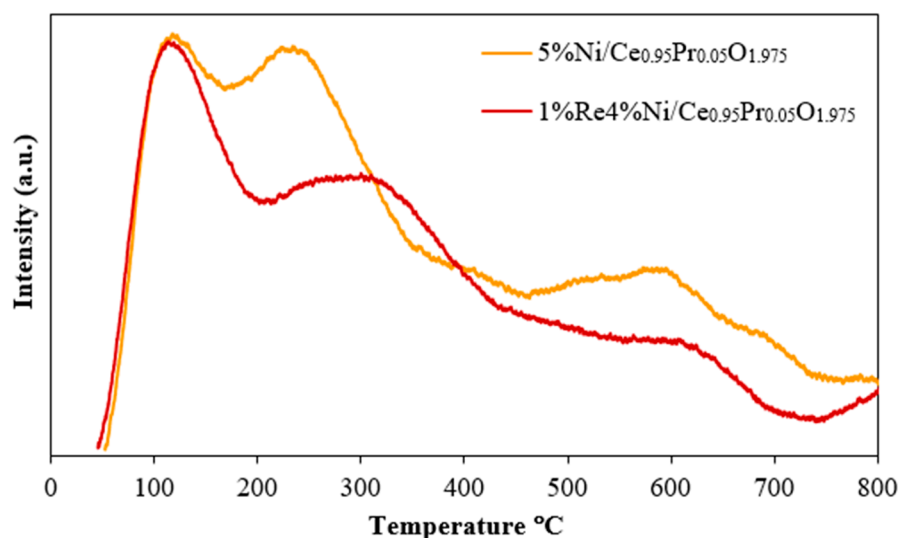


Figure 5. NH₃-TPD of monometallic Ni and bimetallic NiRe supported by Pr-doped ceria.

XPS characterization was used to investigate the surface chemical states of the catalysts. Figure 6a shows the O 1s XPS spectra of 5%Ni/Ce_{0.95}Pr_{0.05}O_{1.975} and 1%Re4%Ni/Ce_{0.95}Pr_{0.05}O_{1.975} catalysts. Three different types of oxygen species were detected in all samples. The detected peaks near 529 eV (O_L), 532 eV (O_A), and 533 eV (O_H) are attributed to lattice oxygen in metal oxide, chemically adsorbed oxygen on the surface, and a surface hydroxyl oxygen species, respectively. The ratios of O_A/O_L, which are calculated from the area of each peak, are an indicator of active oxygen vacancies on the surface [50,51]. XPS results indicated that active oxygen vacancies were higher for the 1%Re4%Ni/Ce_{0.95}Pr_{0.05}O_{1.975} (O_A/O_L = 0.28) compared to 5%Ni/Ce_{0.95}Pr_{0.05}O_{1.975} catalysts (O_A/O_L = 0.24). Therefore, the bimetallic ReNi catalyst tended to display greater activity due to it producing more vacancies or defects.

5%Ni/Ce_{0.95}Pr_{0.05}O_{1.975} and 1%Re4%Ni/Ce_{0.95}Pr_{0.05}O_{1.975} illustrated Ni 2p spectra mainly contributed by Ni²⁺ species at around 855 and 856 eV with a minor content of Ni⁰ species at around 853 eV (Figure 6b). All samples were reduced with 5%H₂/N₂ at 400 °C for 1 hour before XPS measurement. Ni species in the reduced catalysts were in the form of metallic Ni. Furthermore, the different Ni species co-existed due to the interaction with CeO₂-based materials. Metallic Ni⁰ was indicated to be the dominant active species in accelerating the reactants with content of 36.6% and 23.3% in 1%Re4%Ni/Ce_{0.95}Pr_{0.05}O_{1.975} and 5%Ni/Ce_{0.95}Pr_{0.05}O_{1.975} catalysts, respectively. Therefore, the increase in metallic Ni amount in the bimetallic ReNi catalyst implies a superior catalytic performance of Ni catalyst by the addition of Re.

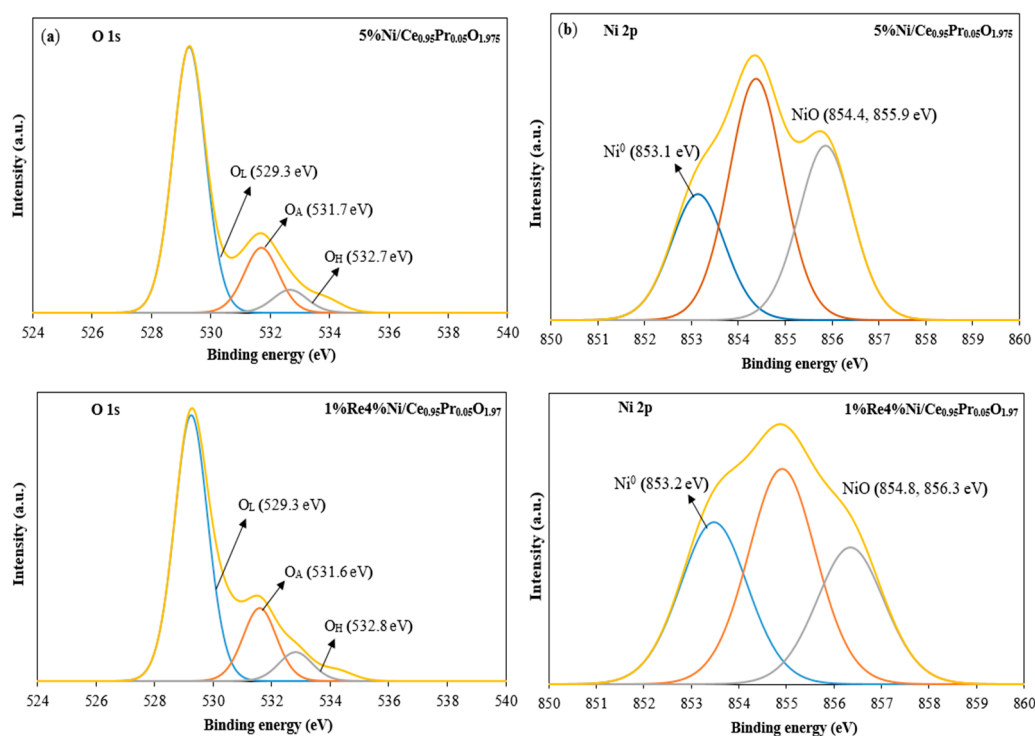


Figure 6. XPS spectra of reduced catalysts before the reaction in 5%Ni/Ce_{0.95}Pr_{0.05}O_{1.975} and 1%Re4%Ni/Ce_{0.95}Pr_{0.05}O_{1.975} for O 1s (a) and Ni 2p (b).

SEM analysis (shown in Figure 7) confirms there was almost no carbon deposition on the surface for the used 1%Re4%Ni/Ce_{0.95}Pr_{0.05}O_{1.975} catalyst. Wang et al. [52] reported that more carbon was deposited and accumulated on the surface of monometallic Ni catalysts during steam reforming of biomass tar, whereas bimetallic NiFe catalysts suppressed the carbon deposition on the surface of the reacted catalyst. Therefore, using bimetallic catalysts could prevent coke formation on the catalysts by providing oxidation of the accumulated carbon.

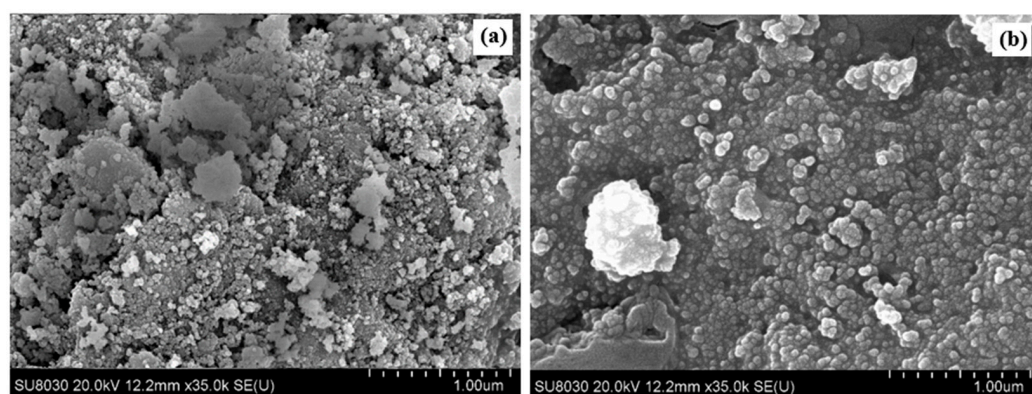


Figure 7. SEM results of (a) fresh and (b) used 1%Re4%Ni/Ce_{0.95}Pr_{0.05}O_{1.975} catalysts.

The carbon deposition of the spent catalysts was evaluated by TG analysis (Figure 8). The oxidation of the carbon deposition in the air leads to weight loss. Small weight loss at low temperatures (below 200 °C) was ascribed to the elimination of moisture and volatile species [53]. The mass loss in the range of 200–400 °C was ascribed to the thermal decomposition of physisorbed carbonaceous species or soft-coke. A major weight reduction between 400 and 600 °C was due to the bulky carbonaceous products or hard coke on the used catalysts. The weight loss percentages of the bulky carbonaceous species on

monometallic Ni and bimetallic NiRe catalysts were 11.6% and 6.2% for 5%Ni/CeO₂ and 1%Re4%Ni/Ce_{0.95}Pr_{0.05}O_{1.975}, respectively, indicating that carbon decomposition decreases when use Pr as dopant and Re as metal additives.

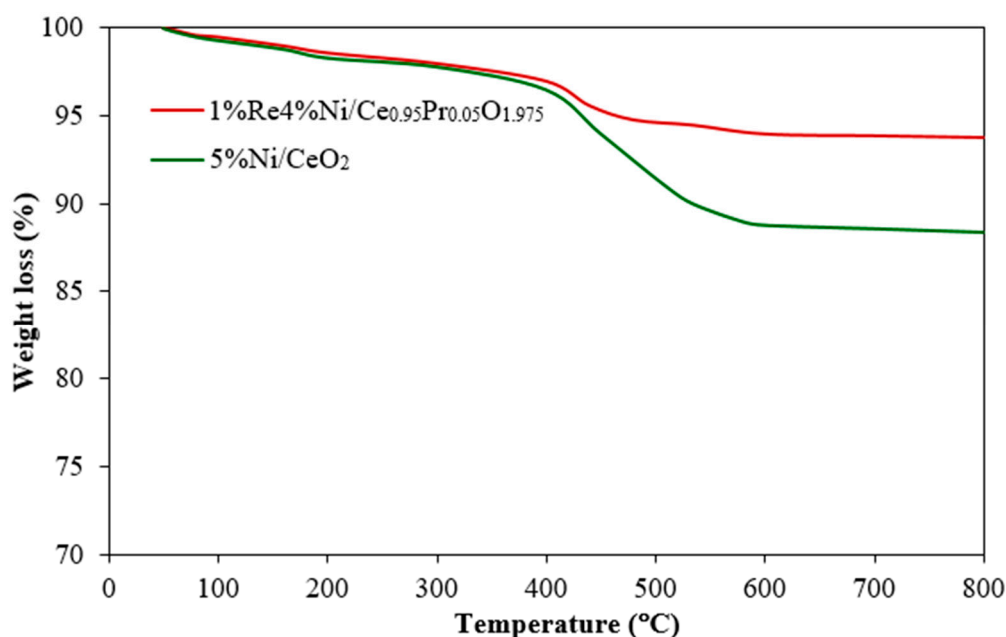


Figure 8. Thermo-gravimetric analysis of the used catalysts.

2.2. Water–Gas Shift Activity and Stability

Figure 9 exhibits the %CO conversion of Ni/CeO₂, Ni/Ce_{0.95}Pr_{0.05}O_{1.975}, and ReNi/Ce_{0.95}Pr_{0.05}O_{1.975}. From previous studies, it was found that further addition of Re does not further raise the rate of water–gas shift reaction, and the optimal content of Re that is enough to maximize the water–gas shift rate is 1 wt. [54]. When attention is drawn to the variation in Sm amount [12], it appears that the Ni catalyst with 5%Sm-doped CeO₂ gives the highest water–gas shift activity. The enhancement of Sm content to 15 wt.% leads to a lowering of nickel dispersion. This result is due to the agglomeration of samarium at a high amount. Therefore, 5% doping amount and 1% of Re metal additives were used in this work to maximize the WGS performance. For Ni/CeO₂, the CO conversion started above 150 °C and ascended slowly to reach the maximum conversion of 84% at 350 °C. As observed, the highest CO conversion was achieved over a bimetallic NiRe/CePrO catalyst, reaching 96% CO conversion at 330 °C with a WGS activity higher than the activities of the monometallic catalysts. NiRe/Ce_{0.95}Pr_{0.05}O_{1.975} has been determined as an excellent catalyst due to its high surface acidity, nickel metal dispersion, and nickel surface area which can enhance the concentration of CO adsorption on the catalyst surface. Furthermore, the NiRe/Ce_{0.95}Pr_{0.05}O_{1.975} catalyst produced more oxygen vacancies, which could increase the redox ability, causing higher WGS activity.

Figure 10 presents the CO₂ and CH₄ selectivity of Ni/Ce_{0.95}Pr_{0.05}O_{1.975} and ReNi/Ce_{0.95}Pr_{0.05}O_{1.975} in the temperature range of 300–500 °C. 1%Re4%Ni/Ce_{0.95}Pr_{0.05}O_{1.975} was exhibited to be an excellent catalyst in terms of WGS activity and selectivity of CO₂ and CH₄. Methane is an unwanted product because it is a precursor for coke formation and competes against H₂ generation. As observed, 5%Ni/Ce_{0.95}Pr_{0.05}O_{1.975} generates CH₄ at low temperatures, whereas 1%Re4%Ni/Ce_{0.95}Pr_{0.05}O_{1.975} is highly selective toward the WGS reaction throughout the investigated temperature. Thus, the incorporation of Re onto Ni/Ce_{0.95}Pr_{0.05}O_{1.975} increased CO conversion at the same time that it suppressed CH₄ formation.

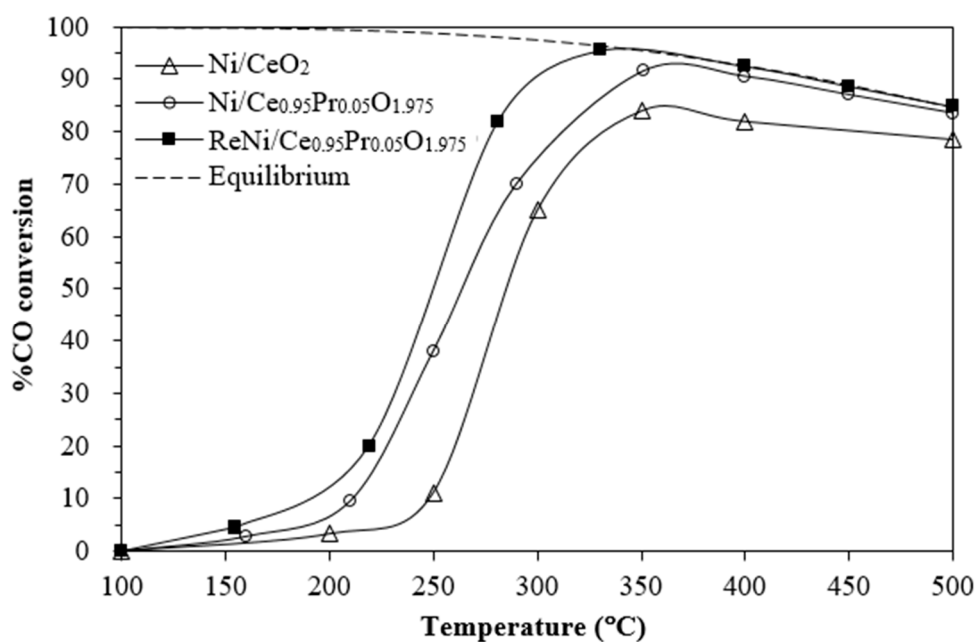


Figure 9. %CO conversion of supported Ni catalysts.

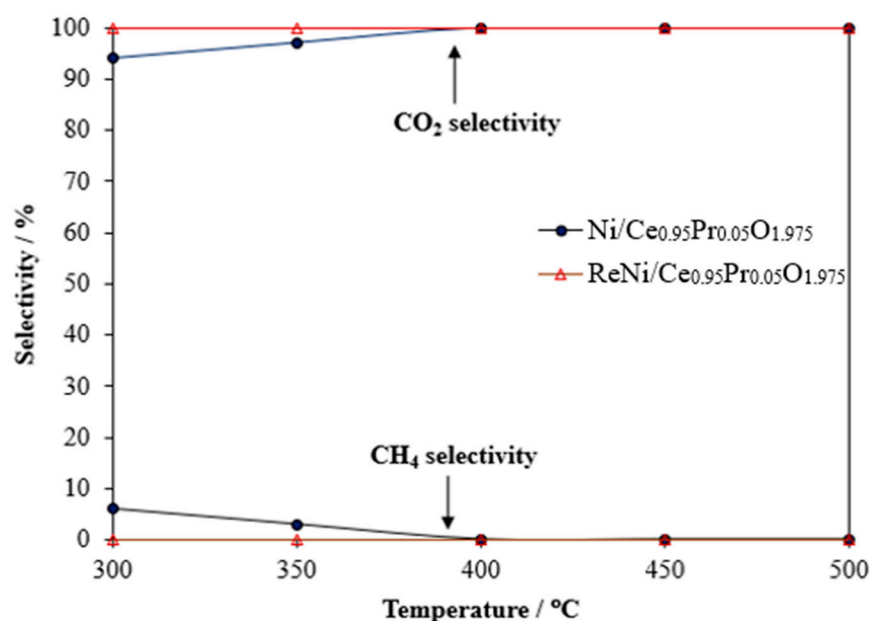


Figure 10. Selectivity to CO₂ and CH₄ as a function of temperature over supported Ni catalysts.

The water–gas shift stability has been performed on the most active catalyst, ReNi/Ce_{0.95}Pr_{0.05}O_{1.975}, under the feed mixture containing 5% CO, 10% H₂O, and 85% N₂ at 300 °C. As shown in Figure 11, the ReNi/Ce_{0.95}Pr_{0.05}O_{1.975} catalyst retained a high CO conversion of about 89% during the first 20 h on stream. Then, the CO conversion slightly decreases to 82% after 60 h of reaction. Hence, the bimetallic ReNi supported by Pr-doped CeO₂ is resistant toward deactivation during a water–gas shift reaction.

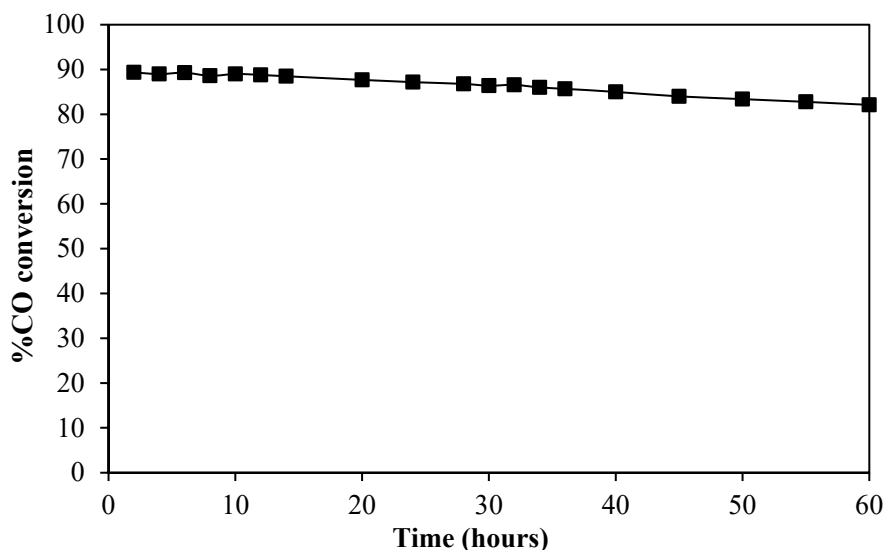


Figure 11. Long-term stability test at 300 °C of 1%Re4%Ni/Ce_{0.95}Pr_{0.05}O_{1.975}.

3. Experimental Procedure

3.1. Catalysts Preparation

A combustion technique was used to synthesize pure CeO₂, and ceria–praseodymia mixed oxides supports with Ce(NO₃)₃·6H₂O (Sigma-Aldrich, Pte. Ltd., Singapore) and Pr(NO₃)₃·6H₂O (Sigma-Aldrich, Pte. Ltd., Singapore) as starting materials. Urea was utilized as a fuel to ignite the reaction. The redox reactions between NH₂CONH₂ and metal nitrates provide the exothermicity essential for the nucleation and growth of the metal oxide powders [55]. Metal nitrate was mixed with urea using a stoichiometry between urea and metal nitrates as 1:2.5. Stirring a mixture obtained a homogeneous solution and then heating with a Bunsen burner until autoignition occurred. CeO₂ and ceria–praseodymia mixed oxides powders were obtained by the thermal decomposition of nitrate and other organic compounds [56].

Ni(NO₃)₂·6H₂O (Alfa Aesar, Thermo Fisher Scientific Inc, Seoul, Republic of Korea) and NH₄ReO₄ (Sigma-Aldrich, Pte. Ltd., Singapore) were used as the metal precursors for the preparation of Ni/CeO₂, Ni/Ce_{0.95}Pr_{0.05}O_{1.975}, and ReNi/Ce_{0.95}Pr_{0.05}O_{1.975} via impregnation method. A solution of nickel and rhenium was added to ceria and ceria–praseodymia mixed oxides powders. All catalysts were dried at 100 °C for 12 h and calcined at 650 °C for 8 h.

3.2. Catalyst Characterization

The specific surface areas of all catalysts were measured by N₂ adsorption–desorption isotherms at 77 K using the BELSORP-MAX instrument (ITS Co. Ltd., Bangkok, Thailand). The samples were outgassed at 300 °C for 3 hours before the analysis. The Brunauer–Emmett–Teller method was utilized to estimate the specific surface areas of the catalysts.

X-ray powder diffraction (XRD) was performed using a PANalytical X'Pert Pro diffractometer (Malvern Panalytical Ltd., Malvern, UK) with the filtered radiation of a copper anode in the range temperature of 20–80°. The X-ray diffractograms were collected using the current of 40 mA and 40 kV with 0.02° per step and 0.5 s per step. The crystallite sizes of CeO₂ were estimated from the full width at half maximum of the strongest (111) reflection using the Debye–Sherrer equation.

Raman spectra were collected on Perkin-Elmer System 2000 FTIR/FT-Raman (Perkin Elmer, Rodgau, Germany) with argon ion laser irradiation at 532 nm wavelength and 10 mW maximum power. The spectra were recorded over the range of 100–1000 cm^{−1} using an operating spectra resolution of 1.0 cm^{−1} of Raman shift.

The H₂ chemisorption, Temperature Programmed Desorption of Ammonia (NH₃-TPD), and H₂-Temperature Programmed Reduction (H₂-TPR) were performed using a catalyst analyzer BELCAT-B instrument (ITS Co. Ltd., Bangkok, Thailand) equipped with a thermal conductivity detector. The reduction behavior of the samples was studied by H₂-TPR. The catalyst was first heated from room temperature to 120 °C in the He flow, maintained at 120 °C for 30 min, and cooled down to 50 °C under the He flow. The TPR measurement was performed from 50 °C up to 1000 °C with the rate of 10 °C/min under 5% H₂ in argon flow. NH₃-TPD analysis was performed to investigate catalyst acidity. The catalyst was first heated from room temperature to 500 °C in argon flow and cooled down to 50 °C under argon. The catalyst was then exposed to pulse titration by using a loop of a known volume of NH₃ in Ar flow until saturation. NH₃-TPD was finally carried out from 50 to 800 °C with a heating rate of 10 °C/min under argon flow. The H₂ chemisorption was performed to determine the surface area, particle size, and dispersion of Ni metal. The sample was evacuated in the He flow at 40 °C and then reduced at 400 °C for 1 h under H₂ flow (30 mL/min). The reduced catalyst was cooled down to 40 °C under helium flow and followed by volumetric H₂ chemisorption with pure hydrogen. The Ni surface area (S_{Ni}), Ni dispersion (D), and Ni particle size (d_{Ni}) were obtained from the instrument software based on the calculation by the following equation [57,58].

$$D (\%) = V_H \times M_{Ni} \times F / V_m \times W \times 100 \quad (2)$$

$$S_{Ni} (m^2/g) = V_m \times N_A \times F \times A_{Ni} / V_{molar} \quad (3)$$

$$d_{Ni} = 60 \times W / \rho \times S_{Ni} \quad (4)$$

where V_H is the chemisorbed H₂ volume (mL/g), V_m is the molar volume of H₂ (mL/mol), W is % wt. of nickel, M_{Ni} is the atomic weight of nickel (g/mol), A_{Ni} is the cross-sectional area of nickel atom (m²/atom), ρ is the density of Ni (g/mL), N_A is Avogadro's number, and F is the stoichiometry factor (the number of active metal atoms to which one adsorbate gas molecule can attach).

Scanning electron microscopy (SEM) was performed on an FE-SEM (HITACHI SU-8030, Hitachi High-Technologies Corporation, Tokyo, Japan) with high vacuum mode using secondary electrons and an acceleration of 30 kV. Energy dispersive X-ray spectroscopy (EDX) was used in conjunction with scanning electron microscopy for the elemental analysis.

Thermo-gravimetric analysis was performed using a Perkin-Elmer TGA/DTA 6300 instrument (Perkin Elmer, Rodgau, Germany) under an airflow rate of 100 mL/min. The content of carbon deposition on the used catalysts was investigated. The mass change in Ni-based catalysts was measured as a function of temperatures up to 800 °C with a heating rate of 20 °C/min.

3.3. Water–Gas Shift Activity

The water–gas shift activity was measured at the temperature from 100 to 500 °C. The catalyst (150 mg) was placed inside a fixed bed flow reactor (310 stainless steel, 0.6 cm outside diameter) between two layers of quartz wool. The catalyst was reduced under 5% H₂ in N₂ flow at 300 °C for an hour before the WGS activity testing. H₂O was fed through a pre-heater using a syringe pump, whereas the flow rates of CO and N₂ were controlled by a mass flow controller. A mixed gas containing 5% CO, 10% H₂O, and 85% N₂ was fed into the reactor. The total flow rate was maintained at 100 mL/min in all testing conditions. The composition of the gas mixture leaving the reactor was determined using an online Shimadzu GC-14B gas chromatography equipped with a thermal conductivity detector (TCD) and a ShinCarbon ST column. Argon is used as the eluent for a ShinCarbon ST column to detect the H₂, CO, and CH₄ at the rate of 50 mL/min. The concentration

of CO, CO₂, and CH₄ at the outlet was repeated at least four times for each analysis. The water–gas shift activities can be calculated according to the following equation:

$$\%CO \text{ conversion} = \frac{CO_{in} - CO_{out}}{CO_{in}} \times 100 \quad (5)$$

where CO_{in} is the inlet molar flow rate of CO (mol s⁻¹) and CO_{out} is the outlet molar flow rate of CO (mol s⁻¹).

4. Conclusions

The influence of Re and Pr on the catalytic activity of Ni/CeO₂ was studied. The incorporation of Re and Pr into Ni/CeO₂ increased the WGS efficiency when compared with Ni/CeO₂. An addition of Pr to Ni/CeO₂ reduced the crystallite size of CeO₂, increased the BET surface area, and promoted higher dispersion of nickel on the CeO₂ surface. Furthermore, the role of rhenium on the water–gas shift performance of supported Ni catalyst was also considered. The results revealed that the addition of rhenium onto Ni/Ce_{0.95}Pr_{0.05}O_{1.975} increased the catalytic performance toward the water–gas shift reaction and suppressed CH₄ formation. The role of rhenium in improving the catalytic activity was due to an increase in surface acidity, Ni surface area, and Ni dispersion, which facilitate CO adsorption on the catalyst surface. Additionally, the acidic character of the catalyst can accelerate CO₂ desorption, leaving behind free active sites for the adsorption of CO and H₂O reactants in subsequent reaction cycles. Moreover, the enhancement of oxygen vacancy concentrations alerts the redox processes at the catalyst surface, which contributes to improving the WGS rate.

Author Contributions: Conceptualization, W.S. and P.T.; methodology, W.S. and P.T.; validation, P.T.; formal analysis, W.S. and P.T.; investigation, P.T.; resources, W.S. and P.T.; data curation, P.T.; writing—original draft preparation, W.S. and P.T.; writing—review and editing, P.T.; supervision, P.T.; funding acquisition, W.S. and P.T. All authors have read and agreed to the published version of the manuscript.

Funding: This study was supported by Thammasat University Research Fund, Contract No. TUFT29/2566 and Thammasat University Research Unit in smart materials from biomass.

Institutional Review Board Statement: Not applicable.

Informed Consent Statement: Not applicable.

Data Availability Statement: Data are contained within the article.

Conflicts of Interest: The authors declare no conflict of interest.

References

1. Wang, H.; Lei, Q.; Li, P.; Liu, C.; Xue, Y.; Zhang, X.; Li, C.; Yang, Z. Key CO₂ capture technology of pure oxygen exhaust gas combustion for syngas-fueled high-temperature fuel cells. *Int. J. Coal Sci. Technol.* **2021**, *8*, 383–393. [[CrossRef](#)]
2. Molochas, C.; Tsiakaras, P. Carbon Monoxide Tolerant Pt-Based Electrocatalysts for H₂-PEMFC Applications: Current Progress and Challenges. *Catalysts* **2021**, *11*, 1127. [[CrossRef](#)]
3. Kim, K.; Yoo, J.D.; Lee, S.; Bae, M.; Bae, J.; Jung, W.; Han, J.W. A Simple Descriptor to Rapidly Screen CO Oxidation Activity on Rare-Earth Metal-Doped CeO₂: From Experiment to First-Principles. *ACS Appl. Mater. Interfaces* **2017**, *9*, 15449–15458. [[CrossRef](#)] [[PubMed](#)]
4. Kayaalp, B.; Lee, S.; Klauke, K.; Seo, J.; Nodari, L.; Kornowski, A.; Jung, W.; Mascotto, S. Template-free mesoporous La_{0.3}Sr_{0.7}Ti_{1-x}FexO_{3±δ} for CH₄ and CO oxidation catalysis. *Appl. Catal. B Environ.* **2019**, *245*, 536–545. [[CrossRef](#)]
5. Montini, T.; Melchionna, M.; Monai, M.; Fornasiero, P. Fundamentals and Catalytic Applications of CeO₂-Based Materials. *Chem. Rev.* **2016**, *116*, 5987–6041. [[CrossRef](#)] [[PubMed](#)]
6. Rodriguez, J.A.; Grinter, D.C.; Liu, Z.; Palomino, R.M.; Senanayake, S.D. Ceria-based model catalysts: Fundamental studies on the importance of the metal–ceria interface in CO oxidation, the water–gas shift, CO₂ hydrogenation, and methane and alcohol reforming. *Chem. Soc. Rev.* **2017**, *46*, 1824–1841. [[CrossRef](#)] [[PubMed](#)]
7. Atribak, I.; Such-Basáñez, I.; Bueno-López, A.; García, A. Comparison of the catalytic activity of MO₂ (M = Ti, Zr, Ce) for soot oxidation under NO_x/O₂. *J. Catal.* **2007**, *250*, 75–84. [[CrossRef](#)]

8. Aneggi, E.; de Leitenburg, C.; Trovarelli, A. On the role of lattice/surface oxygen in ceria–zirconia catalysts for diesel soot combustion. *Catal. Today* **2012**, *181*, 108–115. [[CrossRef](#)]
9. Damyanova, S.; Pawelec, B.; Arishtirova, K.; Huerta, M.M.; Fierro, J. Study of the surface and redox properties of ceria–zirconia oxides. *Appl. Catal. A Gen.* **2008**, *337*, 86–96. [[CrossRef](#)]
10. Hernández, W.Y.; Centeno, M.A.; Romero-Sarria, F.; Odriozola, J.A. Synthesis and Characterization of $Ce_{1-x}Eu_xO_{2-x/2}$ Mixed Oxides and Their Catalytic Activities for CO Oxidation. *J. Phys. Chem. C* **2009**, *113*, 5629–5635. [[CrossRef](#)]
11. Lomonaco, J.G.; Sesuk, T.; Charojrochkul, S.; Tepamatr, P. Effect of Re Addition on the Water–Gas Shift Activity of Ni Catalyst Supported by Mixed Oxide Materials for H₂ Production. *Catalysts* **2023**, *13*, 959. [[CrossRef](#)]
12. Tojira, O.; Tepamatr, P. Catalytic Activity of Ni Based Materials Prepared by Different Methods for Hydrogen Production via the Water Gas Shift Reaction. *Catalysts* **2023**, *13*, 176. [[CrossRef](#)]
13. Atribak, I.; Bueno-López, A.; García-García, A. Thermally stable ceria–zirconia catalysts for soot oxidation by O₂. *Catal. Commun.* **2008**, *9*, 250–255. [[CrossRef](#)]
14. Atribak, I.; Bueno-López, A.; García-García, A. Role of yttrium loading in the physico-chemical properties and soot combustion activity of ceria and ceria–zirconia catalysts. *J. Mol. Catal. A Chem.* **2009**, *300*, 103–110. [[CrossRef](#)]
15. Kirkgeçit, R.; Torun, H.; Dokan, F.K.; Öztürk, E. Optical and electrical conductivity properties of rare earth elements (Sm, Y, La, Er) co-doped CeO₂. *J. Rare Earths* **2021**, *40*, 1619–1627. [[CrossRef](#)]
16. Reddy, B.M.; Saikia, P.; Bharali, P.; Yamada, Y.; Kobayashi, T.; Muhler, M.; Grünert, W. Structural Characterization and Catalytic Activity of Nanosized Ceria-Terbia Solid Solutions. *J. Phys. Chem. C* **2008**, *112*, 16393–16399. [[CrossRef](#)]
17. Somacescu, S.; Parvulescu, V.; Calderon-Moreno, J.M.; Suh, S.-H.; Osiceanu, P.; Su, B.-L. Uniform nanoparticles building Ce_{1-x}Pr_xO_{2-δ} mesoarchitectures: Structure, morphology, surface chemistry, and catalytic performance. *J. Nanoparticle Res.* **2012**, *14*, 885. [[CrossRef](#)]
18. Zhang, G.; Zhao, Z.; Xu, J.; Zheng, J.; Liu, J.; Jiang, G.; Duan, A.; He, H. Comparative study on the preparation, characterization and catalytic performances of 3DOM Ce-based materials for the combustion of diesel soot. *Appl. Catal. B Environ.* **2011**, *107*, 302–315. [[CrossRef](#)]
19. Rodriguez, J.A.; Hanson, J.C.; Kim, J.-Y.; Liu, G.; Iglesias-Juez, A.; Fernández-García, M. Properties of CeO₂ and Ce_{1-x}Zr_xO₂ Nanoparticles: X-ray Absorption Near-Edge Spectroscopy, Density Functional, and Time-Resolved X-ray Diffraction Studies. *J. Phys. Chem. B* **2003**, *107*, 3535–3543. [[CrossRef](#)]
20. Wang, X.; Hanson, J.C.; Liu, G.; Rodriguez, J.A.; Iglesias-Juez, A.; Fernández-García, M. The behavior of mixed-metal oxides: Physical and chemical properties of bulk Ce_{1-x}Tb_xO₂ and nanoparticles of Ce_{1-x}Tb_xO_y. *J. Chem. Phys.* **2004**, *121*, 5434–5444. [[CrossRef](#)]
21. Ryan, K.M.; McGrath, J.P.; Farrell, R.A.; O’Neill, W.M.; Barnes, C.J.; Morris, M.A. Morris, Measurements of the lattice constant of ceria when doped with lanthana and praseodymia—the possibility of local defect ordering and the observation of extensive phase separation. *J. Phys. Condens. Matter* **2003**, *15*, L49. [[CrossRef](#)]
22. Poggio-Fraccari, E.; Irigoyen, B.; Baronetti, G.; Mariño, F. Ce-Pr mixed oxides as active supports for Water-gas Shift reaction: Experimental and density functional theory characterization. *Appl. Catal. A Gen.* **2014**, *485*, 123–132. [[CrossRef](#)]
23. Poggio-Fraccari, E.; Baronetti, G.; Mariño, F. Pr³⁺ surface fraction in CePr mixed oxides determined by XPS analysis. *J. Electron Spectrosc. Relat. Phenom.* **2018**, *222*, 1–4. [[CrossRef](#)]
24. Mariño, F.; Descorme, C.; Duprez, D. Supported base metal catalysts for the preferential oxidation of carbon monoxide in the presence of excess hydrogen (PROX). *Appl. Catal. B Environ.* **2005**, *58*, 175–183. [[CrossRef](#)]
25. Hung, C.-M. The effect of the calcination temperature on the activity of Cu–La–Ce composite metal catalysts for the catalytic wet oxidation of ammonia solution. *Powder Technol.* **2009**, *191*, 21–26. [[CrossRef](#)]
26. Chen, Y.-Z.; Liaw, B.-J.; Chen, H.-C. Selective oxidation of CO in excess hydrogen over CuO/Ce_xZr_{1-x}O₂ catalysts. *Int. J. Hydrogen Energy* **2006**, *31*, 427–435. [[CrossRef](#)]
27. Ratnasamy, C.; Wagner, J.P. Water Gas Shift Catalysis. *Catal. Rev.* **2009**, *51*, 325–440. [[CrossRef](#)]
28. Kim, S.H.; Chung, J.H.; Kim, Y.T.; Han, J.; Yoon, S.P.; Nam, S.W.; Lim, T.-H.; Lee, H.-I. SiO₂/Ni and CeO₂/Ni catalysts for single-stage water gas shift reaction. *Int. J. Hydrogen Energy* **2010**, *35*, 3136–3140. [[CrossRef](#)]
29. Hilaire, S.; Wang, X.; Luo, T.; Gorte, R.; Wagner, J. A comparative study of water-gas-shift reaction over ceria supported metallic catalysts. *Appl. Catal. A Gen.* **2001**, *215*, 271–278. [[CrossRef](#)]
30. Poggio-Fraccari, E.; Mariño, F.; Laborde, M.; Baronetti, G. Copper and nickel catalysts supported on praseodymium-doped ceria (PDC) for the water-gas shift reaction. *Appl. Catal. A Gen.* **2013**, *460–461*, 15–20. [[CrossRef](#)]
31. Wang, T.; Porosoff, M.D.; Chen, J.G. Effects of oxide supports on the water-gas shift reaction over PtNi bimetallic catalysts: Activity and methanation inhibition. *Catal. Today* **2014**, *233*, 61–69. [[CrossRef](#)]
32. Wang, D.; Li, Y.; Wen, L.; Xi, J.; Liu, P.; Hansen, T.W.; Li, P. Ni-Pd-incorporated Fe₃O₄ yolk-shelled nanospheres as efficient magnetically recyclable catalysts for reduction of n-containing unsaturated compounds. *Catalysts* **2023**, *13*, 190. [[CrossRef](#)]
33. Wen, L.; Wang, D.; Xi, J.; Tian, F.; Liu, P.; Bai, Z.-W. Heterometal modified Fe₃O₄ hollow nanospheres as efficient catalysts for organic transformations. *J. Catal.* **2022**, *413*, 779–785. [[CrossRef](#)]
34. Guo, X.; Li, M.; Qiu, L.; Tian, F.; He, L.; Geng, S.; Liu, Y.; Song, Y.; Yang, W.; Yu, Y. Engineering electron redistribution of bimetallic phosphates with CeO₂ enables high-performance overall water splitting. *Chem. Eng. J.* **2023**, *453*, 139796. [[CrossRef](#)]

35. Iida, H.; Igarashi, A. Difference in the reaction behavior between Pt–Re/TiO₂ (Rutile) and Pt–Re/ZrO₂ catalysts for low-temperature water gas shift reactions. *Appl. Catal. A Gen.* **2006**, *303*, 48–55. [[CrossRef](#)]
36. Lomonaco, J.G.; Tojira, O.; Charojrochkul, S.; Tepamatr, P. Structure-Activity Relationship of Ceria Based Catalyst for Hydrogen Production. *Chiang Mai J. Sci.* **2022**, *49*, 1129–1134. [[CrossRef](#)]
37. Tepamatr, P.; Laosiripojana, N.; Charojrochkul, S. Water gas shift reaction over monometallic and bimetallic catalysts supported by mixed oxide materials. *Appl. Catal. A Gen.* **2016**, *523*, 255–262. [[CrossRef](#)]
38. Tojira, O.; Lomonaco, J.G.; Sesuk, T.; Charojrochkul, S.; Tepamatr, P. Enhancement of hydrogen production using Ni catalysts supported by Gd-doped ceria. *Heliyon* **2021**, *7*, e08202. [[CrossRef](#)]
39. Saw, E.T.; Oemar, U.; Ang, M.L.; Kus, H.; Kawi, S. High-temperature water gas shift reaction on Ni–Cu/CeO₂ catalysts: Effect of ceria nanocrystal size on carboxylate formation. *Catal. Sci. Technol.* **2016**, *6*, 5336–5349. [[CrossRef](#)]
40. Tsakoumis, N.E.; Walmsley, J.C.; Rønning, M.; van Beek, W.; Rytter, E.; Holmen, A. Evaluation of Reoxidation Thresholds for γ -Al₂O₃-Supported Cobalt Catalysts under Fischer–Tropsch Synthesis Conditions. *J. Am. Chem. Soc.* **2017**, *139*, 3706–3715. [[CrossRef](#)]
41. D’angelo, A.M.; Chaffee, A.L. Correlations between Oxygen Uptake and Vacancy Concentration in Pr-Doped CeO₂. *ACS Omega* **2017**, *2*, 2544–2551. [[CrossRef](#)] [[PubMed](#)]
42. Taniguchi, T.; Watanabe, T.; Sugiyama, N.; Subramani, A.K.; Wagata, H.; Matsushita, N.; Yoshimura, M. Identifying Defects in Ceria-Based Nanocrystals by UV Resonance Raman Spectroscopy. *J. Phys. Chem. C* **2009**, *113*, 19789–19793. [[CrossRef](#)]
43. Lee, Y.; He, G.; Akey, A.J.; Si, R.; Flytzani-Stephanopoulos, M.; Herman, I.P. Raman Analysis of Mode Softening in Nanoparticle CeO_{2- δ} and Au–CeO_{2- δ} during CO Oxidation. *J. Am. Chem. Soc.* **2011**, *133*, 12952–12955. [[CrossRef](#)] [[PubMed](#)]
44. Guo, M.; Lu, J.; Wu, Y.; Wang, Y.; Luo, M. UV and Visible Raman Studies of Oxygen Vacancies in Rare-Earth-Doped Ceria. *Langmuir* **2011**, *27*, 3872–3877. [[CrossRef](#)] [[PubMed](#)]
45. Hong, S.J.; Virkar, A.V. Lattice Parameters and Densities of Rare-Earth Oxide Doped Ceria Electrolytes. *J. Am. Ceram. Soc.* **1995**, *78*, 433–439. [[CrossRef](#)]
46. Guo, J.; Lou, H.; Zhao, H.; Chai, D.; Zheng, X. Dry reforming of methane over nickel catalysts supported on magnesium aluminate spinels. *Appl. Catal. A Gen.* **2004**, *273*, 75–82. [[CrossRef](#)]
47. Akiki, E.; Akiki, D.; Italiano, C.; Vita, A.; Abbas-Ghaleb, R.; Chlala, D.; Ferrante, G.D.; Laganà, M.; Pino, L.; Specchia, S. Production of hydrogen by methane dry reforming: A study on the effect of cerium and lanthanum on Ni/MgAl₂O₄ catalyst performance. *Int. J. Hydrogen Energy* **2020**, *45*, 21392–21408. [[CrossRef](#)]
48. Parastayev, A.; Muravev, V.; Osta, E.H.; van Hoof, A.J.F.; Kimpel, T.F.; Kosinov, N.; Hensen, E.J.M. Boosting CO₂ hydrogenation via size-dependent metal–support interactions in cobalt/ceria-based catalysts. *Nat. Catal.* **2020**, *3*, 526–533. [[CrossRef](#)]
49. Sartoretto, E.; Novara, C.; Chiodoni, A.; Giorgis, F.; Piumetti, M.; Bensaid, S.; Russo, N.; Fino, D. Nanostructured ceria-based catalysts doped with La and Nd: How acid-base sites and redox properties determine the oxidation mechanisms. *Catal. Today* **2021**, *390–391*, 117–134. [[CrossRef](#)]
50. Sultana, S.; Mansingh, S.; Scurrill, M.; Parida, K.M. Controlled Synthesis of CeO₂NS–Au–CdSQDs Ternary Nanoheterostructure: A Promising Visible Light Responsive Photocatalyst for H₂ Evolution. *Inorg. Chem.* **2017**, *56*, 12297–12307. [[CrossRef](#)]
51. Mansingh, S.; Padhi, D.K.; Parida, K.M. Enhanced visible light harnessing and oxygen vacancy promoted N, S co-doped CeO₂ nanoparticle: A challenging photocatalyst for Cr(vi) reduction. *Catal. Sci. Technol.* **2017**, *7*, 2772–2781. [[CrossRef](#)]
52. Wang, L.; Li, D.; Koike, M.; Koso, S.; Nakagawa, Y.; Xu, Y.; Tomishige, K. Catalytic performance and characterization of Ni–Fe catalysts for the steam reforming of tar from biomass pyrolysis to synthesis gas. *Appl. Catal. A Gen.* **2011**, *392*, 248–255. [[CrossRef](#)]
53. Sahoo, S.K.; Ray, S.S.; Singh, I. Structural characterization of coke on spent hydroprocessing catalysts used for processing of vacuum gas oils. *Appl. Catal. A Gen.* **2004**, *278*, 83–91. [[CrossRef](#)]
54. Chayakul, K.; Srithanratana, T.; Hengrasmee, S. Effect of Re addition on the activities of Co/CeO₂ catalysts for water gas shift reaction. *J. Mol. Catal. A Chem.* **2011**, *340*, 39–47. [[CrossRef](#)]
55. Takeda, T.; Kato, K.; Kikkawa, S. Gel Combustion Synthesis of Rare Earth Aluminate Using Glycine or Urea. *J. Ceram. Soc. Jpn.* **2007**, *115*, 588–591. [[CrossRef](#)]
56. Tepamatr, P.; Laosiripojana, N.; Sesuk, T.; Charojrochkul, S. Effect of samarium and praseodymium addition on water gas shift performance of Co/CeO₂ catalysts. *J. Rare Earths* **2020**, *38*, 1201–1206. [[CrossRef](#)]
57. Tuti, S.; Luisetto, I.; Laverdura, U.P.; Marconi, E. Dry Reforming of Methane on Ni/Nanorod–CeO₂ Catalysts Prepared by One-Pot Hydrothermal Synthesis: The Effect of Ni Content on Structure, Activity, and Stability. *Reactions* **2022**, *3*, 333–351. [[CrossRef](#)]
58. Di Michele, A.; Dell’Angelo, A.; Tripodi, A.; Bahadori, E.; Sánchez, F.; Motta, D.; Dimitratos, N.; Rossetti, I.; Ramis, G. Steam reforming of ethanol over Ni/MgAl₂O₄ catalysts. *Int. J. Hydrogen Energy* **2018**, *44*, 952–964. [[CrossRef](#)]

Disclaimer/Publisher’s Note: The statements, opinions and data contained in all publications are solely those of the individual author(s) and contributor(s) and not of MDPI and/or the editor(s). MDPI and/or the editor(s) disclaim responsibility for any injury to people or property resulting from any ideas, methods, instructions or products referred to in the content.